Available online at website: https://journal.bcrec.id/index.php/bcrec

Bulletin of Chemical Reaction Engineering & Catalysis, 21 (4) 2026, xxx-xxx

Original Research Article

Potential Conversion of Chicken Bone Waste into Fe_2O_3-Functionalized Hydroxyapatite Photocatalyst

Septiana Intan Permata[1,2], Is Fatimah[1,2*], Nunung Nurlela[1,2], Zakiyya Salma Hamidah[1,2], Suresh Sagadevan[3], Azlan Kamari[4], Won-Chun Oh[5], Deblina Roy[6], Ruey-an Doong[6]

[1]Department of Chemistry, Faculty of Mathematics and Natural Sciences, Universitas Islam Indonesia, Kampus Terpadu UII, Jl. Kaliurang Km 14, Sleman, Yogyakarta 55584, Indonesia.
[2]Nanotechnology and Sustainable Chemistry Research Centre, Universitas Islam Indonesia, Laboratorium Kimia, Kampus Terpadu UII, Jl. Kaliurang Km 14, Sleman, Yogyakarta 55584, Indonesia.
[3]Nanotechnology & Catalysis Research Centre, University of Malaya, Kuala Lumpur 50603, Malaysia.
[4]Faculty of Sciences and Mathematics, Universiti Pendidikan Sultan Idris, Tanjong Malim, Perak, Malaysia.
[5]Department of Advanced Materials Science and Engineering, Hanseo University, Seosan-si 356-706, Korea.
[6]Department of Biomedical Engineering and Environmental Sciences, National Tsing Hua University, Hsinchu, 30013, Taiwan.

Received: 16th June 2026; Revised: 20th August 2026; Accepted: 22th August 2026
Available online: 30th August 2026; Published regularly: December 2026

Abstract

Functional material of iron oxide (Fe_2O_3) nanoparticles-functionalized Hydroxyapatite (HA) was synthesized from chicken bone waste. The preparation of material involved the calcination of chicken bone waste followed by the dispersion of iron oxide precursors and hydrothermal treatment to get coprecipitated HA. Systematic physicochemical characterization was performed by various analytical techniques, including scanning electron microscopy, transmission electron microscopy, X-ray diffraction, Raman spectroscopy, and diffuse reflectance UV-Visible spectroscopy. The photocatalytic activity of the composite was examined to degrade methylene blue under various photon sources and pH condition. The results demonstrated that a high crystalline Fe_2O_3/HA was derived, and detail of the analysis confirm the functionality of iron as dopant in the crystalline structure of HA and the dispersed photoactive nanoparticles. Photocatalytic degradation experiments resumed that the high degradation efficiency could be achievable at alkaline condition and under visible light illumination, as the efficiency of 74.46% was the optimum value.

Keywords: Dye photodegradation; Fe_2O_3; Hydroxyapatite; Photocatalyst; Chicken Bone

How to Cite: Permata, S. I., Fatimah, I., Nurlaela, N., Hamidah, Z., Sagadevan, S., Kamari, A., Oh, W., Roy, D., Doong, R. (2026). Potential Conversion of Chicken Bone Waste into Fe_2O_3-Functionalized Hydroxyapatite Photocatalyst. *Bulletin of Chemical Reaction Engineering & Catalysis*, 21 (4), xxx-xxx. (DOI: 10.9767/bcrec.20778)

Permalink/DOI: https://doi.org/10.9767/bcrec.20781

1. Introduction

The progression of industrialization and technology has made human life easier. However, the use of various chemicals in industry also results in the release of chemical substances as toxic waste that has the potential to harm the natural ecosystems environment. Among some chemicals used in industries, dyes are applied in various industrial processes, including the textile, printing, pigment and paint manufactures. Dyes are characterized by their persistent properties imposing significant adverse impacts on aquatic systems [1]. Advanced oxidation process (AOPs) is a well-known method to treat dye-contaminated water, as it has advantageous compared to adsorption such as fast, complete, and no further treatments required. Within the method, photocatalytic oxidation is a promising technique with due to its ability to completely degrade a wide range of organic pollutants into harmless end products such as CO_2 and H_2O [2]. The

* Corresponding Authors.
Email: isfatimah@uii.ac.id (I. Fatimah)

technique involves the use of semiconductor photocatalysts that capable to catch photon and generate electron-hole pairs for furthermore creating reactive oxidative species (ROS). The ROS species can break down complex and persistent contaminants, including dyes. Advances in development of photocatalyst is to improve photocatalytic efficiency and support the photocatalytic mechanism by adsorption. The combination of semiconductor photocatalyst with porous materials as photoactive support is one of the strategies to this scheme [3,4].

Hydroxyapatite (HA) has emerged as an effective support material for photocatalysts due to its high surface area, biocompatibility, chemical stability, and tuneable surface properties. As a calcium phosphate-based material, HA provides abundant active sites for anchoring semiconductor photocatalysts such as TiO_2, ZrO_2, NiO, ZnO. Previous works reported that the combination of metal oxide facilitating improved dispersion and preventing particle agglomeration. This enhanced distribution increases the availability of reactive sites and promotes more efficient light absorption and charge separation. Additionally, the porous structure of hydroxyapatite enables better adsorption of pollutants, bringing them into proximity with the photo catalytically active species [5].

From the sustainability perspective, HA could be derived by extracting from biowaste. HA was successfully prepared from fish bone, cow bone, and chicken bone, and the functionalization with metal oxide demonstrated absorptivity and catalytic activity [6–9]. Considering that chicken bone is an abundant food waste in many countries, utilization of chicken bone as raw material for HA to be support for photocatalysis applications is potentially developed. In advance, selection of low-cost metal oxide such as iron oxide photocatalyst as functionalization agent is an economically beneficial and could be a sustainable material with a concept of waste to functional resource. Based on these backgrounds, in this study, the composite of Fe_2O_3-supported hydroxyapatite composites (Fe_2O_3/HA) were synthesized using chicken bones as a source of natural hydroxyapatite. Photocatalytic activity of the composite was examined to methylene blue (MB) dye, referring to its vast utilization in industries.

2. Materials and Method

2.1 Materials

The chicken bone waste used in this study was collected from nearby restaurants and food stalls in Sleman District, Yogyakarta Province, Indonesia. A total of 500 grams of chicken bones were first cleaned of meat and soft tissue residues to remove organic contaminants that could interfere with the calcination process and reduce the purity of the final product. Cleaning was performed under running water to remove fat, blood, and water-soluble impurities. After washing, the bones were dried in an oven at 100 °C for 3 days until their moisture content was reduced. The dried bone was then calcined in a furnace at a temperature of 1000 °C for 2 hours to get CaO. The solid obtained from these steps was then mechanically ground using a mortar and pestle. Some chemicals consisted of $FeCl_3.6H_2O$, MB, $(NH_4)_2HPO_4$, isopropanol (IPR), ethylene diamine tetra acetate (EDTA), and benzoquinone (BQ), and AgCl were purchased from Merck (Darmstadt, Germany) and used without purification.

2.2. Preparation of Fe_2O_3/HA

The Fe_2O_3/HA nanocomposite was prepared by dissolving 3.65 grams of $FeCl_3 \cdot 6H_2O$ in deinozed water. Furthermore, into the mixture, about 1 wt% of surfactant cetyltrimethylammonium bromide (CTAB) was added, followed by stirring for 3 hours at 45 °C to achieve homogenization. Into the mixture, 7.4 g of derived CaO was added to 100 mL of deinozed water. Furthermore, the $(NH_4)_2HPO_4$ solution was slowly added into the mixture with set up Ca/P of 1.67 under stirring and nitrogen gas (N_2) was bubbled through it. Subsequently, the NaOH solution was added to adjust the pH of solution =11. The resulting precursor precipitate was then transferred into a Teflon-lined autoclave and heated at 150 °C for 24 h. The result from these steps was a slurry which furthermore dried and calcined at 500 °C for 2 h. For comparison purpose, the HA synthesis without the addition of iron precursors was performed.

2.3. Physicochemical Characterization

Scanning electron microscopy (SEM Hitachi SU 8020 UHR FESEM) was employed to analyze the morphology of material coupled with and Horiba EDX Spectrometer for elemental composition. The spectra of XRD were recorded on Rigaku (Ni-filtered Cu Kα, λ = 1.5406A, 30 kV and 25 mA) scanned the 2θ between 20˚ and 70˚ and the step size of 0.02˚ 2θ per second. High–resolution transmission electron microscopy (HR–TEM) (JEM–2100, JEOL, Tokyo, Japan). Raman spectrum was recorded on Renishaw Via Raman Microscope Laser Wavelength: 514 nm. Optical property of magnetic biochar was determined on Diffuse reflectance UV-Visible JASCO VSM 760, while photoluminescence spectroscopic analysis was performed using Horiba iHR320. Electrochemical impedance spectroscopy (EIS) analysis were recorded by employing an AC

voltage of 5 mV amplitude with the initial potencial at 0.4 v (vs. Ag/AgCl) over the frequency range from 100 kHz to 100 mHz without light illumination.

2.4. Photocatalytic Activity Examination

The synthesized Fe_2O_3/HA was examined as photocatalyst for MB degradation. Particularly, Fe_2O_3/HA powder was dispersed in an aqueous solution of MB (5 mg L^{-1}) with catalyst dosage of 0.8 g/L. Prior the photon illumination, stirring of the mixture in the dark for 15 min was proceeded to achieve adsorption–desorption equilibrium. Furthermore, the photon was exposed into the suspension, and the sampling was collected every 15 min subsequently. Micro filtration was performed before the samples were analysed using a UV–VIS spectrophotometer (UV–2080, Shimazu, Kyoto, Japan). Effect of photon source (UV and visible light) and pH of solution were explored as factors affecting degradation. The degradation efficiency (%) in photocatalytic activity test was calculated using the following Eq. (1):

$$Degradation\ efficiency\ (DE,\%) = \frac{C_0 - C_t}{C_0}\ x\ 100 \quad (1)$$

with C_o and C_t are the initial concentration of MB and concentration at sampling time t. Figure 1 represents the scheme of material's preparation, characterization and photocatalytic activity examination.

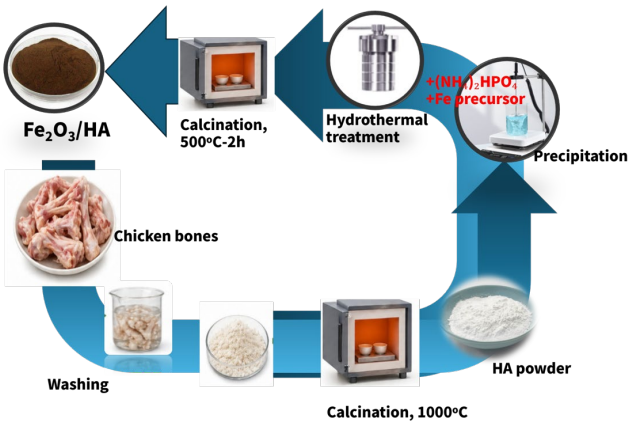

Figure 1. Scheme of Fe_2O_3/HA preparation.

3. Results and Discussion

Figure 2 shows the SEM images of HA and Fe_2O_3/HA, and also the EDX spectrum of Fe_2O_3/HA. HA demonstrates the spherical in mixture with heterogenous forms and size of the particles, meanwhile the Fe_2O_3/HA exhibits a rougher surface with the dispersed tiny particles. EDX analysis result confirms the Fe content of 5.45 % in the Fe_2O_3/HA as additional component of HA which dominantly consist of calcium and phosphor elements (Table 1).

The elemental mapping represents an evolution of the atomic dispersion which iron is identified. Further investigation using HRTEM shows the multiple crystallographic orientations of the particles. The particles size is distributed with the size ranging at 5-100 nm and the mean of 38 nm (Figure 3b). By using more intensive analysis, the image shows the lattice fringes with

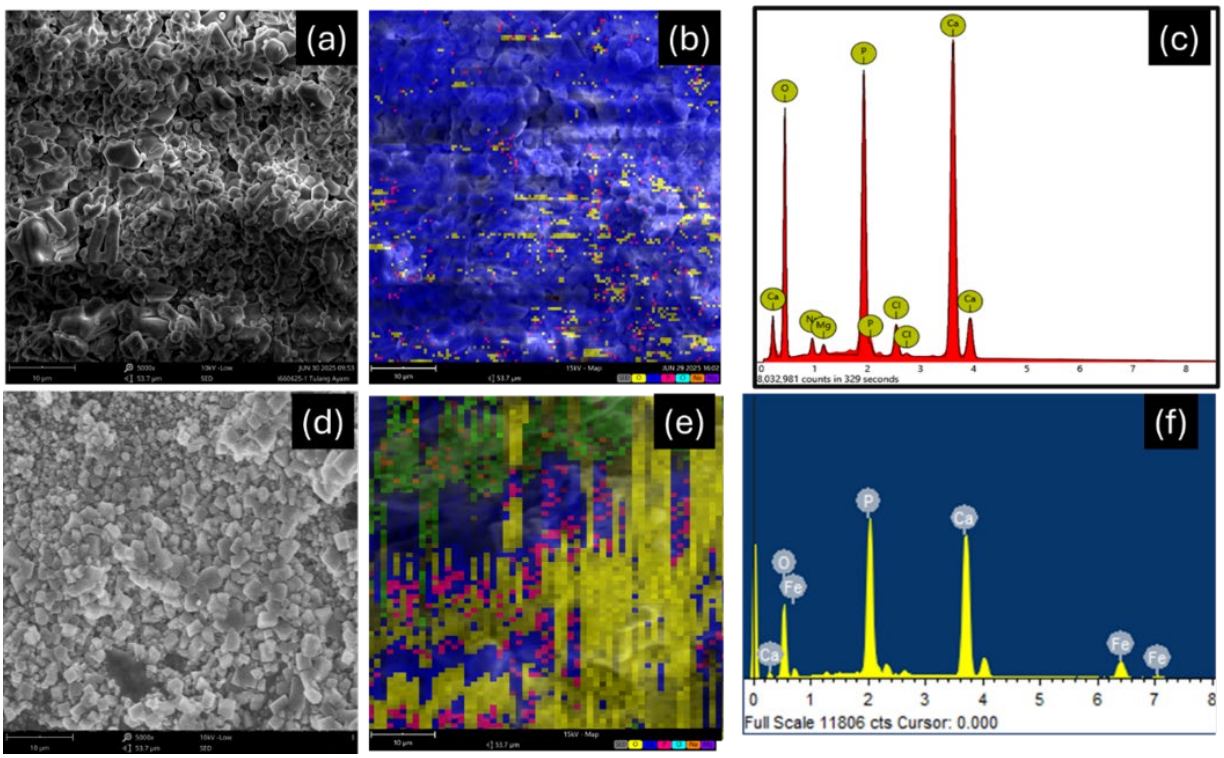

Figure 2. SEM image, elemental mapping, and EDX spectrum of (a-c) HA, (d-f) Fe_2O_3/HA.

measured interplanar spacings of 0.281 nm associated to the peak indexed to (211) peak of HA (Figure 3e) [10,11], and the darker spots includes the particles showing the measured interplanar spacings of 0.25 nm which is associated to the peak indexed to (110) reflection of α-Fe_2O_3 (Figure 3f) [12,13]. These data confirm the presence of Fe_2O_3 as photoactive site in the nanocomposite which plays role in photocatalysis mechanism.

X-ray diffraction (XRD) characterisation was performed to determine the crystal structure and phases formed in the synthesised material. The hydroxyapatite (HA) sample exhibits sharp diffraction peaks at 2θ angles of 25.89°, 31.63°, 32.31°, 32.67°, 39.48°, 46.71°, 49.47° and 53.23° in the XRD pattern shown in Figure 4. These correspond to the crystal planes (002), (211), (112), (300), (310), (222), (213) and (004) of hydroxyapatite. According to JCPDS File No. 09-0432 [14], these peaks are characteristic of the hexagonal crystal structure of hydroxyapatite. This indicates that the main phase formed in the sample is highly crystalline hydroxyapatite, characterised by strong intensity on the (211) plane at around 31.63°. Additional peaks are observed at 33.12°, 35.61°, and 44.51° that are associated to the presence of the hematite phase (α-Fe_2O_3) which is in consistence to 104), (110), and (116) reflections referred to JCPDS File No. 33-0664. The HA peaks in Fe_2O_3/HA exhibit a slight decrease in FWHM or broader compared to HA, indicating an increase in lattice strain due to the substitution of the smaller Fe^{3+} ion (0.64 Å) for Ca^{2+} (0.99 Å). This effect indicates that Fe has been partially doped into the HA matrix, while

Table 1. Elemental analysis of Fe_2O_3/HA.

Element	Content (wt.%)	
	HA	Fe_2O_3/HA
O K	46.02	53.01
P K	17.05	17.67
Ca K	36.9	22.37
Fe K	n.d	6.95

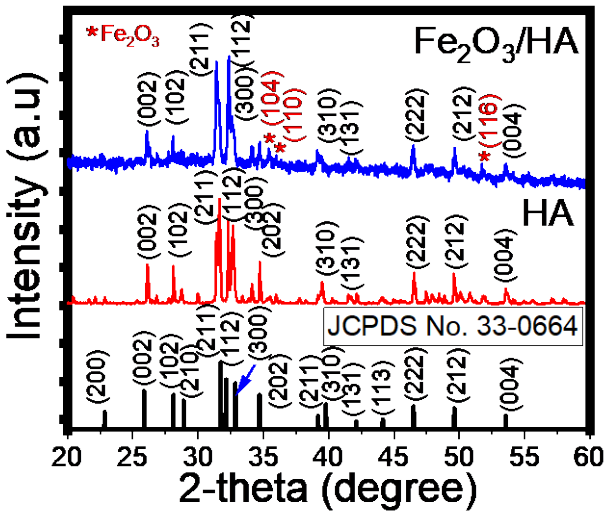

Figure 4. XRD pattern of Fe_2O_3/HA in comparison to HA and JCPDS File No. 33-0664

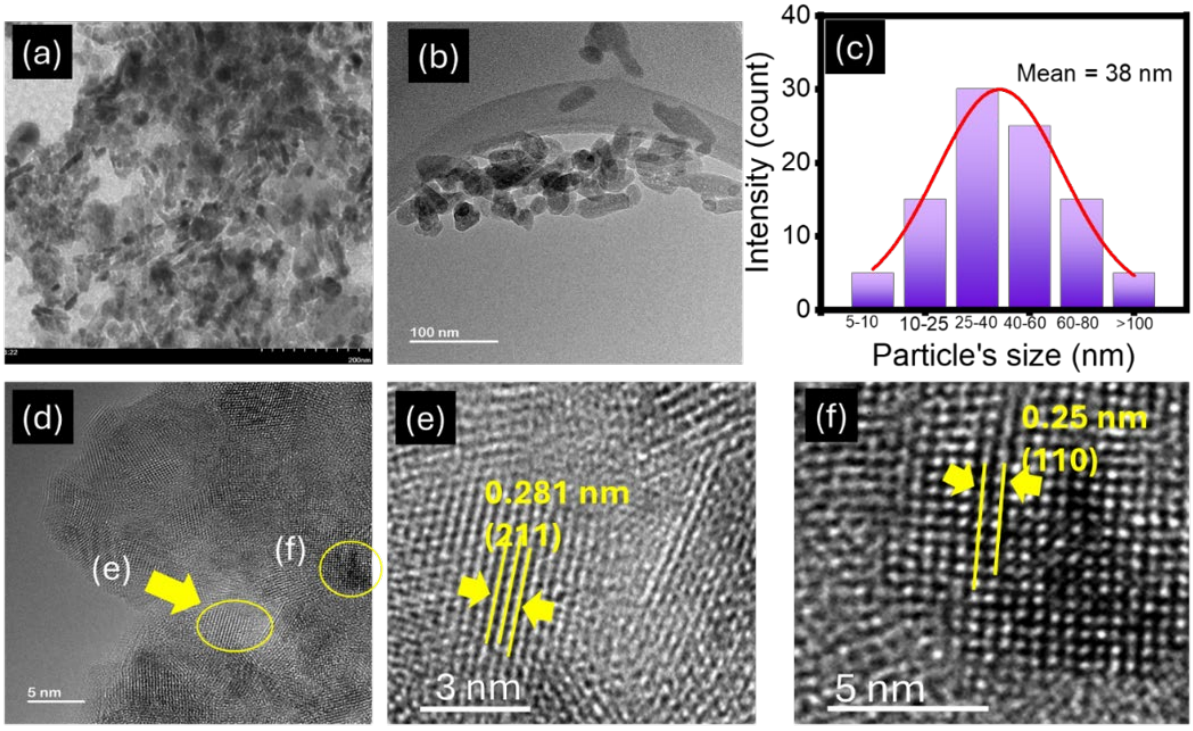

Figure 3. (a-b) TEM images in different magnification, c. Particle's size distribution, (d-f) HRTEM of Fe_2O_3/HA.

simultaneously forming a hematite phase dispersed on its surface [15].

In addition to phase identification, XRD analysis can also be used to quantitatively determine crystallinity parameters, including the lattice parameter (a), average crystallite size (L), X-ray density (ρXRD), and stretching absorption bonds (v1 and v2) of HA, and the data are presented in Table 1. The crystallite size (L) was based on the Scherrer equation (Eq. 2.):

$$D = \frac{K\lambda}{\beta \, Cos \, \theta} \quad (2)$$

where D is the average crystallite size (nm), λ is the X-ray wavelength (1.5406 Å), β is the full width at half maximum (FWHM), and θ is the diffraction angle.

Based on the data in Table 2, the average crystal size of hydroxyapatite (HA) was 54.19 nm, whereas in the Fe_2O_3/HA composite it increased to 77.00 nm. Both values remain within the nanomaterial size range (1–100 nm). This is associated to the lattice parameters (a and c) which in Fe_2O_3/HA these are larger, implying the less compressive strength in the crystal. This is also reflected by lower density of the increase in crystal size in Fe_2O_3/HA compared to pure HA indicates that the presence of Fe_2O_3/HA compared to HA. However, the stretching absorption bands (v_1 and v_2) of both samples are in same position, suggests that the bonding among atoms in the composite is in same stability. Due to inappreciable peak of Fe_2O_3, it is concluded that Fe_2O_3 particles are available on the HA surface, and from the crystallographic data, the Fe precursor was influenced the HA structure through crystal growth.

The Raman technique was employed to identify the structural analysis of HA and Fe_2O_3/HA. As shown in Figure 5, HA shows the intensive peak positioned at ~960 cm^{-1} representing P-O stretching vibration (v_1), which is the primary fingerprint band for crystalline hydroxyapatite, supported by lower intense peak around 1400-1800 cm^{-1} associated to the triply degenerate asymmetric P–O stretching mode (v_3), and the bending vibration positioned at ~400-450 cm^{-1} corresponding to P-O-P linkage [16]. The P-O stretching vibration remained in Fe_2O_3/HA, suggesting the maintained HA structure, with additional peaks around 222-596 cm^{-1}. In details, the band positioned at 222 cm^{-1} represents A_{1g} mode from the symmetric stretching of iron, which is associated with the band of E_g mode at 286 cm^{-1} from the Fe-O bending vibration. Additionally, E_g and A_{1g} modes are expressed by the bands at 400 cm^{-1} and 506 cm^{-1}, while the band at 596 cm^{-1} is associated with asymmetric stretching of lattice oxygen network. The results are pointing that the dispersed Fe_2O_3 onto HA exhibits electrochemically active to the exposed energy which supports its applications in surface active interactions and photocatalysis [17].

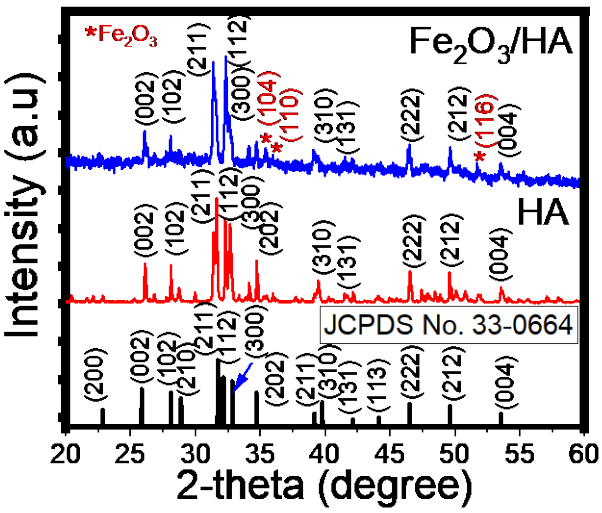

Figure 4. XRD pattern of Fe_2O_3/HA in comparison to HA and JCPDS File No. 33-0664

Table 2. Lattice parameter (a), average crystallite size (L), X-ray density (ρXRD), oxygen positional parameter (u), and stretching absorption bonds (v1 and v2) of HA.

Parameter	HA	Fe_2O_3/HA
a (Å)	4.79	4.87
c (Å)	5.54	5.62
L (nm)	54.19	77.00
ρXRD (g/cm^3)	15.12	14.46
v_1 (cm^{-1})	490	490
v_2 (cm^{-1})	470	470

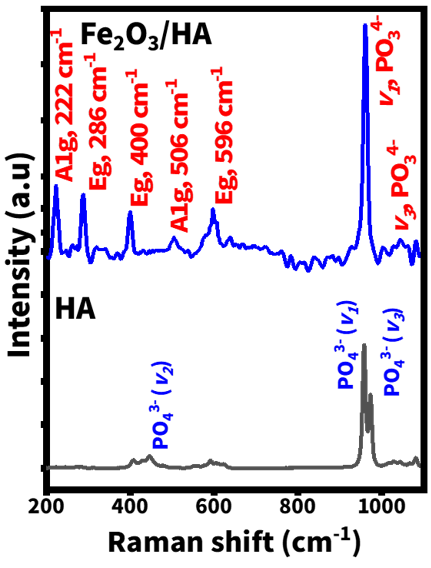

Figure 5. Raman spectra of Fe_2O_3/HA in comparison with HA.

Optical characterization was performed using UV-DRS to determine the band gap energy (E_g) of the synthesized material. The diffuse reflectance data obtained from the spectrophotometer was converted into the Kubelka–Munk function, defined as (Eq. 3):

$$F(R) = \frac{(1-R)^2}{2R} \quad (3)$$

Where R is the reflectances value. This Kubelka–Munk function $(F(R))$ is considered proportional to the optical absorption coefficient (α), so it can be applied to the following Tauc's equation (Eq. 4):

$$(\alpha h\nu)^n = A(h\nu - E_g) \quad \text{(eq.4)}$$

With, $h\nu$ = photon energy (eV), A = proportionality constant, n = index depending on the type of electronic transition, n = 1/2 for direct allowed transitions, and n = 2 for indirect allowed transitions.

Diffuse-reflectance UV-Visible spectroscopy analysis was performed to investigate the optical properties of the Fe_2O_3/HA sample. From the spectrum (Figure 6a), it could be resumed that Fe_2O_3/HA has capability to absorb light within the visible and UV range with higher absorbance at UV range. The Tauc's plot calculated from the by plotting of $(F(R)h\nu)^2$ with respect to hv presented in Figure 6b demonstrate the edge wavelength positioned at 495 nm, which is associated to a bandgap energy of 2.5 eV. The photoluminescence (PL) spectrum presented in Figure 6c gives the indication of emission bands centered at approximately 340 nm and 445 nm. The emission at around 340 nm could be related to the surface defect-related radiative recombination, while the emission positioned at 445 nm which associated to the energy of around 2.79 eV is the representation of electronic transition of Fe^{2+} with oxygen vacancy in Fe_2O_3 structure. The peaks imply that Fe_2O_3/HA could facilitate charge-carrier separation and prolong the lifetime of photogenerated electrons and holes, which is a crucial process in the for photocatalytic mechanism. This indicates the success of the dispersion of Fe_2O_3 as the charge transfer representing formation of intermediate energy levels resulting from the interaction of Fe 3d orbitals with O 2p orbitals in the phosphate group (PO_4^{3-}) within the HA lattice. The capability of Fe_2O_3/HA to transfer electron is reflected by by EIS analysis (Figure 6d). Compared to Fe_2O_3, Fe_2O_3/HA demonstrates the smaller Nyquist semicircle diameter corresponds to a narrower band gap energy, expressed by the progressive electron-hole transport and a reduced recombination rate [18,19]. These results are in consistence with the study on Fe_2O_3/HA composite having the band gap energy of 2.20–2.50 eV [20]. In addition, HA has the band gap

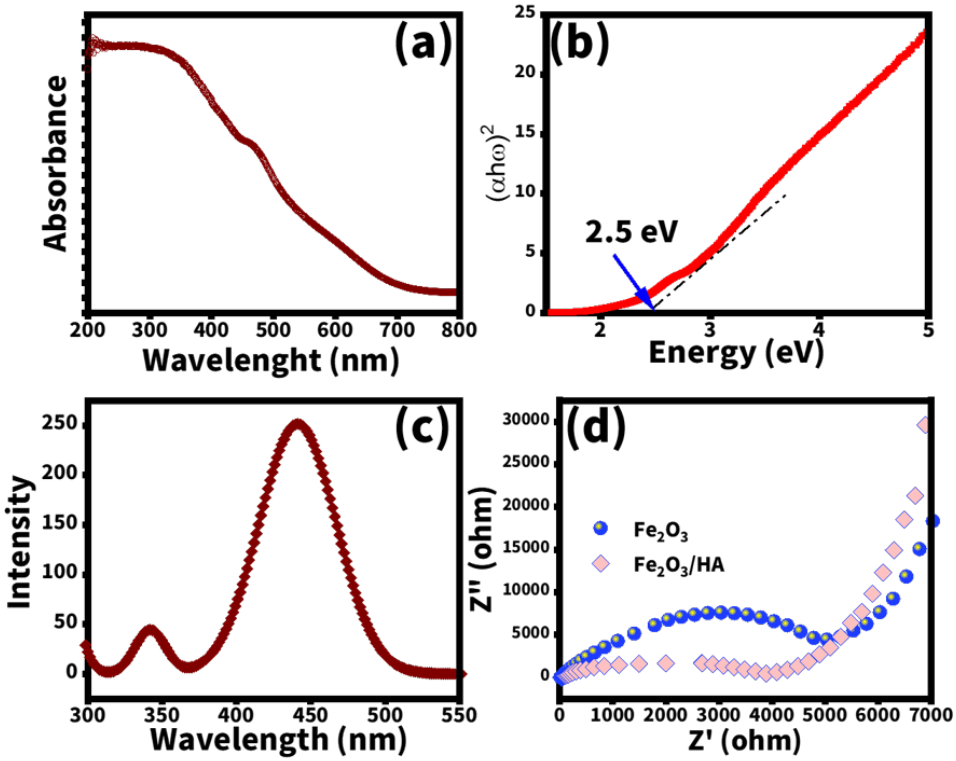

Figure 6. a. UV-DRS spectrum, b. Tauc's plot of Fe_2O_3/HA, c. PL spectrum of Fe_2O_3/HA, and d. EIS spectra of Fe_2O_3/HA in comparison to Fe_2O_3

energy ranging at 4-5.0 which behaves as an insulator, so it performs no photocatalytic activity [21].

3.1. Photocatalytic Activity Examination

The photocatalytic (PC) activity of Fe_2O_3/HA was examined for MB degradation at two varied pH of 6 and 10, and at varied photon source of visible and UV light. The plots presented in Figure 7a and 7b show the decreased concentration represented by $[C/C_0]$ along the time of reaction in comparison with the adsorption (Ads) and photolytic treatments. In this case, the photolytic treatments are the light (UV and visible) exposure to MB solution without the presence of photocatalyst. The resumed degradation efficiency (*DE*) depicted in Figure 7c implies the significant increase of MB removal over PC system respect to adsorption process. In detail the highest removal is achievable by PC under UV at pH of 10 system (78.88%), followed by the PC process using visible light at pH of 10 (57%). Compared to PC procedure at pH of 6, the basic condition leads to faster reaction which the PC procedure under UV and visible light exposure give the *DE* of 37.44% and 44.42%, respectively. Even though the photolytic procedures at both varied pH show insignificant concentration change with the *DE* less than 2%, these phenomena are possibly related to that the basic condition provided $^{-}$OH in producing more •OH. The light exposure initiates the electron excitation to leave hole (h^+) which produces •OH by its interaction with $^{-}$OH. From compared light source, the more h^+ created by UV light exposure rather than visible light, corresponding to the higher energy provided by UV for sufficiently create the excitation. Even though there are insignificant values of *DE* achievable by photolytic procedures, this assumption is also proven by the higher removal obtained by photolytic treatment at pH of 10 rather than at pH of 6. Furthermore, from the kinetics plot at pH of 6, the visible light exposure gives higher *DE* rather than UV light. It means that even though the UV support the photon energy, but the less amount of $^{-}$OH could not significantly contribute to produce comparable amount of •OH as the basic condition. The mechanism is fit to was investigated on Fe_3O_4/HA/Ag nanocomposites for various dyes. It was concluded that degradation process involved several key steps, including absorption of light, generation and separation of electron–hole pairs, and generation of reactive oxygen species (ROS)[20].

Based on the plots, pseudo-first order and pseudo-second-order kinetics were applied to assess the decreased reactant concentration referred to the following equations (Eq. 4 and Eq. 5):

$$ln\frac{C_t}{C_0} = k_1 t \quad (4)$$

$$\frac{1}{C_t} = k_2 t + \frac{1}{C_0} \quad (5)$$

With C_0 and C_t are initial concentration and the MB concentration at time of t, respectively, k_1 and k_2 are apparent kinetics constant of pseudo-first

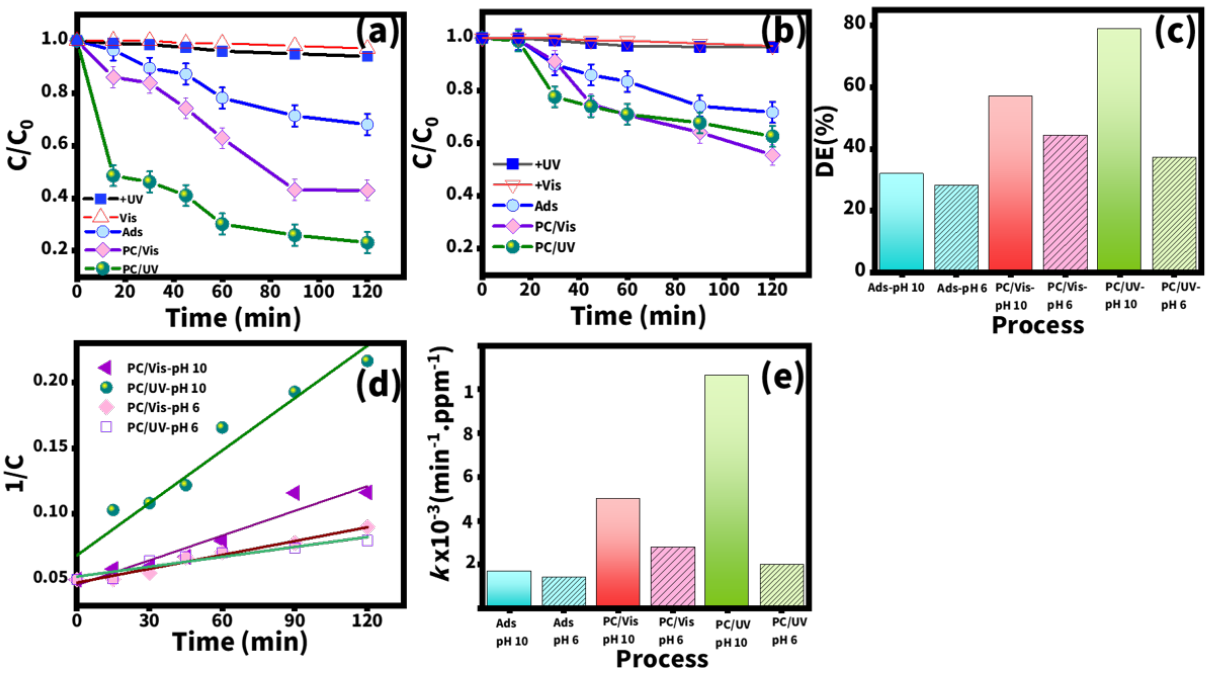

Figure 7. a. Kinetics plots of the process at pH of 10, b. Kinetics plots of the process at pH of 4, c. Recapitulated *DE*, d. Pseudo-second order of PC process using Fe_2O_3/HA, e. Recapitulated k of the PC using Fe_2O_3/HA.

order and pseudo-second order, respectively. The kinetics equations and the parameters are listed in Table 3. Based on RSQ, all of the reaction demonstrated the fitness to both the pseudo-first order and the pseudo-second-order kinetics. However, except for the photocatalytic process under UV light at pH of 10 (PC/UV-pH10), the RSQ of the pseudo-first-order kinetics (0.948) is higher than that of the pseudo-second-order kinetics (0.928). The appropriateness of pseudo-second-order kinetics to the MB adsorption is similar to was reported from the adsorption of MB using hydroxyapatite derived from camel bone [22]. Meanwhile, the photocatalytic degradation of MB using hydroxyapatite-supported WO_3 represented the fitness to the pseudo-second-order kinetics with the equivalent *DE* value for the same MB concentration of 20 mg/L [23], similar was reported using Ag-doped hydroxyapatite[24]. The kinetics plots are provided in Figure 7d, and the resumed apparent kinetics constant (k_2) based on the plots are depicted in Figure 7e. The k_2 values are in line with the resumed *DE* values demonstrating the PC/UV-pH 10 as the superior process with highest k of 1.39×10^{-3} $min^{-1}.ppm^{-1}$. It is observed that the kinetics constant of the MB adsorption at pH of 10 is also higher than the process at pH of 6. Previous studies of photocatalytic degradation over modified hydroxyapatite highlighted the contributed adsorption to the overall photocatalytic mechanism [25–27].

Considering the involvement of adsorption to PC process, synergistic index based on the ratio of the kinetic constant of PC to the individual apparent kinetic constants of adsorption (k_{Ads}) and photolytic process (k_{+UV}) is calculated using the following formula (Eq. 6):

$$Synergistic\ index\ (S_{PC}) = \frac{k_{PC}}{k_{ads}+k_{+UV}} \quad (6)$$

The k values are obtained from the pseudo-second-order equations. The calculations give the S_{PC} of 2.79 and 6.18 for PC process at pH of 10 using visible light and UV light, respectively. Parallelly, the values are 1.75 and 1.30 for the process at pH of 6. The higher S_{PC} obtained at pH 10 exhibits the synergistic combination of the role of photocatalyst surface to adsorb the MB as reactant and the involvement of photolytic mechanism. It could be concluded that the photocatalytic mechanism composed by the combination surface interaction among photocatalyst, the presence of photocatalyst, light energy, and capability of photocatalyst to absorb light.

Referred to previous references and the accelerated reaction at high amount of ^{-}OH, the mechanism of photocatalytic reaction process can be described by the following reactions:

$Fe_2O_3 + hv \rightarrow Fe_2O_3\ (h^+ + e^-)$
$e^- + O_2 \rightarrow \bullet O_2$
$h^+ + OH^- \rightarrow \bullet OH$
$H_2O \longrightarrow H^+ + {}^-OH$
$\bullet OH + O_2 \rightarrow \bullet OOH$
$\bullet OH + MB \rightarrow$ degradation products ($CO_2 + H_2O$)
$\bullet OOH + MB \rightarrow$ degradation products ($CO_2 + H_2O$)

Table 3. Kinetic parameters of methylene blue photodegradation using Fe_2O_3/HA catalyst under variations of light source and pH.

Process/Photon source-pH	Kinetic Equation (First Order)	R^2	Kinetic Equation (Second Order)	k ($min^{-1}.ppm^{-1}$)	R^2
Ads-pH 10	$ln\frac{C}{C_0} = 1.98x10^{-3} - 3.44x10^{-3}t$	0.972	$\frac{1}{C} = 2.11x10^{-4}t + 3.04x10^{-2}$	$2.11x10^{-4}$	0.977
+Vis-pH 10	$ln\frac{C}{C_0} = 3.33x10^{-3} + 2.60x10^{-4}t$	0.940	$\frac{1}{C} = 2.74x10^{-5}t + 4.98x10^{-2}$	$1.36x10^{-5}$	0.945
+UV-pH 10	$ln\frac{C}{C_0} = 3.32x10^{-3} + 2.70x10^{-4}t$	0.945	$\frac{1}{C} = 1.39x10^{-5}t + 4.29x10^{-2}$	$1.39x10^{-5}$	0.947
PC/Vis-pH 10	$ln\frac{C}{C_0} = 2.22x10^{-3} + 7.74x10^{-3}t$	0.951	$\frac{1}{C} = 6.27x10^{-4}t + 3.44x10^{-2}$	$6.27x10^{-4}$	0.924
PC/UV-pH 10	$ln\frac{C}{C_0} = 0.37 - 1.06x10^{-2}t$	0.882	$\frac{1}{C} = 2.39x10^{-3}t + 3.29x10^{-2}$	$2.39x10^{-3}$	0.947
Ads-pH 6	$ln\frac{C}{C_0} = 1.33x10^{-3} + 3.01x10^{-3}t$	0.963	$\frac{1}{C} = 1.79x10^{-4}t + 4.95x10^{-2}$	$1.79x10^{-4}$	0.971
+Vis-pH 6	$ln\frac{C}{C_0} = 3.33x10^{-3} + 2.60x10^{-4}t$	0.940	$\frac{1}{C} = 1.38x10^{-4}t + 3.04x10^{-2}$	$2.11x10^{-4}$	0.977
+UV-pH 6	$ln\frac{C}{C_0} = 3.32x10^{-3} + 2.70x10^{-4}t$	0.945	$\frac{1}{C} = 1.36x10^{-5}t + 4.98x10^{-2}$	$1.36x10^{-5}$	0.945
PC/Vis-pH 6	$ln\frac{C}{C_0} = 1.76x10^{-2} - 5.24x10^{-3}t$	0.956	$\frac{1}{C} = 3.51x10^{-4}t + 4.65x10^{-2}$	$3.51x10^{-4}$	0.972
PC/UV-pH 6	$ln\frac{C}{C_0} = -3.93x10^{-3} - 3.93x10^{-3}t$	0.843	$\frac{1}{C} = 2.51x10^{-4}t + 4.95x10^{-2}$	$2.51x10^{-4}$	0.883

The photocatalytic mechanism could be described as in Figure 8a.

To investigate the occurrence of oxidant species in the mechanism, the effect of scavengers was studied. For radical hydroxyl (•OH), hole (h^+), and superoxide (•OOH) scavengers, IPR, EDTA and BQ were isopropanol (IPR), were utilized, respectively. The kinetics plots and resumed k are demonstrated in chart at Figure 8b. The presence of IPR and BQ supress the reaction rate represented by the reduced DE and *k*, but EDTA enhanced the reaction. Moreover, the reduction caused by BQ is more significant compared to that of IPR. The IPR and BQ imply the role of •OH and •OOH in the mechanism, which, in detail the trapped •OOH more significantly reduces the whole mechanism. In opposite way, EDTA enhances the reaction rate with the most significant difference towards the reaction without scavengers. As EDTA function is to block the h^+, the highest role of h^+ in determining the reaction mechanism is pointed out. This reflects that as the h^+ blocked, the production of $\bullet O_2$ from the interaction between excited electron and O_2 could be more efficient due to the inhibited electron-hole (e^-- h^+) recombination. In this case, a difference phenomenon is observed as from some studies on photocatalysis, usually EDTA scavenger tends to the decreased reaction rate and less influential to the mechanism[28,29]. The condition may be influenced by stabilized electron-hole (e^-- h^+) by the stabilization of the solid support [30].

The activity is approaching to green synthesized Fe_2O_3 nanoparticles with the *DE* of 79% which gained by UV light illumination for

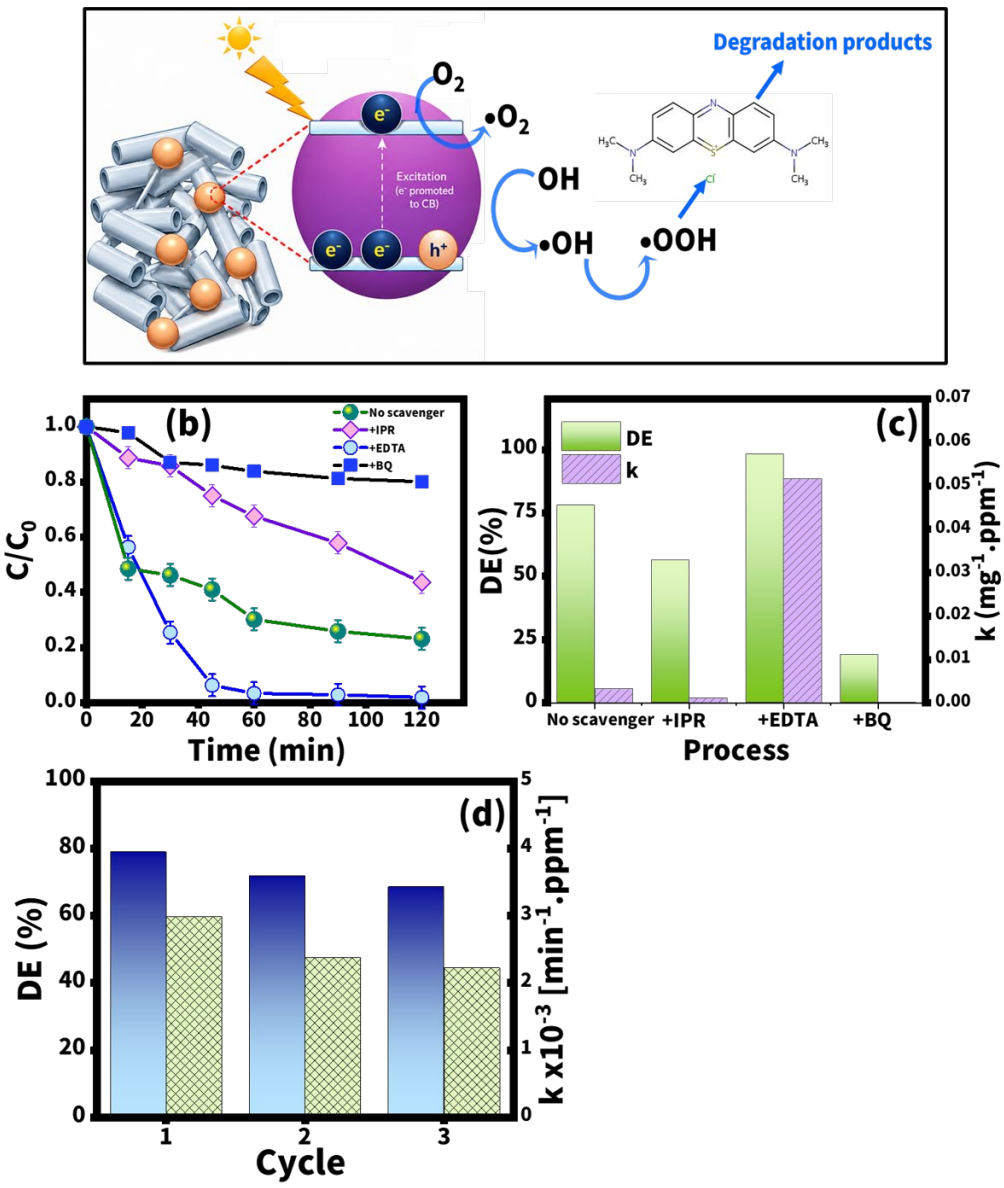

Figure 8. a. Schematic representation of photocatalytic mechanism using Fe_2O^3/HA, b. Kinetics plot of MB degradation at the presence of scavengers, c. Recapitulated *DE* and *k* of degradation with scavengers' addition, d. recapitulated *D* and *k* at recycling..

120 min [31], but much lower compared to Fe_2O_3 nanoparticles prepared by thermal decomposition of $Fe(NO_3)_3{\cdot}3H_2O$ at the presence of malic acid with the *DE* of 98% [32]. The advantage using Fe_2O_3/HA in this work was less energy required as xenon lamp utilized and less amount of photoactive site of Fe_2O_3. The photocatalytic activity of prepared Fe_2O_3/HA in comparison to other Fe_2O_3-based materials for MB degradation is listed in Table 4. Furthermore, the stability of Fe_3O_4/HA was evaluated by measuring the *DE* and *k* of recycling experiments. The recapitulated *DE* and *k* presented in Figure 8d reduces along the recycling as for 3rd cycle, the percentage of reduced *DE* is about 12.5% from the first usage, while *k* reduction is about 25%. The reduction is probably caused by the blockage surface with MB.

In general, the conclusive aspect that gained by this is that the use of chicken bone as source for HA synthesis shows potentiality as support for Fe_2O_3 photoactive material. The photocatalytic activity for MB degradation represents another benefit as a solution for food waste problem valorisation, and at the same time providing functional material for wastewater treatment.

4. Conclusion

In the study, upscaling chicken bone waste into Fe_2O_3-supported hydroxyapatite was successfully performed. The physicochemical characterization was systematically conducted and suggest the high crystallinity of the composite. Identification using XRD, TEM and Raman spectroscopy suggested that an insertion of Fe in hydroxyapatite structure beside of the dispersion of Fe_2O_3 particles on the hydroxyapatite surface was observed. The particle size of prepared nanocomposite is 38 nm with the band gap energy of 2.5 eV. The photocatalytic degradation experimental results showed that the nanocomposite has photoactivity to degrade methylene blue under visible and UV light source. The study revealed the contributing adsorption and surface condition of the photocatalyst material to optimize the oxidation mechanism. The photocatalytic mechanism is influenced by the presence radicals, superoxide radicals and hole, and the reusability test showed the instability for 3 cycles of the process.

Acknowledgment

Please acknowledge especially of Funder of Research as guided here: https://journal.bcrec.id/index.php/bcrec/pages/view/authorguide Section 11.19.

CRedit Author Statement

Author Contributions: Fachrul Rozy: Conceptualization, Methodology, Investigation, Formal Analysis, Writing Original Draft,

Table 4. Compared photocatalytic activity of prepared Fe_2O_3/HA with Fe_2O_3-based photocatalysts for MB degradation.

Material	Reaction condition	*DE* (%)	Reference
Green synthesized Fe_2O_3 nanoparticles	Photocatalyst dosage of 0.01g/L for MB concentration of 10 mg/L, under UV light for 180 min	78.68	[33]
Fe_2O_3	Photocatalyst dosage of 7 mg/100L for MB concentration of 10 mg/L, under UV light for 180 min. Photocatalyst showed stability until 5th use	95	[19]
α-Fe_2O_3 Nanospindles	Photocatalytic degradation of 10 mg/L MB under UV light for 6 h.	78	[34]
Al_2O_3/Fe_2O_3	Photocatalyst dosage of 0.2 g/100 mL for MB 25 mg/L under visible light	75.1	[34]
Ag@Fe_2O_3	Photocatalyst dosage of 0.2 g/200 mL for MB 25 mg/L for 60 min. Reaction obeys pseudo-first order kinetics with k=3.25×10^{-2}/min	97.1	[34]
Fe_2O_3/graphene/CuO	Photocatalyst dosage of 0.5 g/L for MB 25 mg/L for 60 min. Reaction obeys pseudo-first order kinetics. The photocatalyst stable until 5th cycle	81.5	
Fe_2O_3/HA	Photocatalyst dosage of 0.2 g/250 mL for MB 20 mg/L for 120 min. Reaction obeys pseudo-second order kinetics.	78.8	Present work

Editing; Tania Surya Utami: Supervision, Editing and Reviewing; Setiadi: Supervision and Reviewing; Wawan Rustyawan: Supervision and reviewing. All authors have read and agreed to the published version of the manuscript.

References

[1] Goudjil, M.B., Dali, H., Zighmi, S., Mahcene, Z., Bencheikh, S.E. (2024) Photocatalytic degradation of methylene blue dye with biosynthesized Hematite α-Fe2O3 nanoparticles under UV-Irradiation, *Desalination and Water Treatment*, 317. DOI: 10.1016/j.dwt.2024.100079.

[2] Iyyappan, J., Gaddala, B., Gnanasekaran, R., Gopinath, M., Yuvaraj, D., Kumar, V. (2024) Critical review on wastewater treatment using photo catalytic advanced oxidation process : Role of photocatalytic materials , reactor design and kinetics, *Case Studies in Chemical and Environmental Engineering*, 9, 100599. DOI: 10.1016/j.cscee.2023.100599.

[3] Fatimah, I., Fadillah, G., Yanti, I., Doong, R.A. (2022) Clay-Supported Metal Oxide Nanoparticles in Catalytic Advanced Oxidation Processes: A Review, *Nanomaterials*, 12. DOI: 10.3390/nano12050825,

[4] Fatimah, I., Audita, R., Purwiandono, G., Hidayat, H., Sagadevan, S., Oh, W.C., an Doong, R. (2024) In-situ synthesis of hydroxyapatite-supported Ag3PO4 using cockle (Anadara granosa) shell as photocatalyst in rhodamine B photodegradation and antibacterial agent, *Case Studies in Chemical and Environmental Engineering*, 10, 100797. DOI: 10.1016/j.cscee.2024.100797.

[5] Kalita, J., Bharali, L., Dhar, S.S. (2024) Zn supported on hydroxyapatite encapsulated Fe3O4 (Fe3O4/HAp@Zn) nanocomposite for visible light driven photodegradation of ciprofloxacin antibiotics, *Interactions*, 245, 1–19. DOI: 10.1007/s10751-024-02158-8.

[6] Serafim, J.T., Modolon, H.B., Montedo, O.R.K., Alice, M., Cechinel, P., Arcaro, S. (2026) Tilapia Bone-Derived Hydroxyapatite Particles for Controlled Citronella (Cymbopogon nardus) Release and Antimicrobial Activity, journal title?? Vol ??? Issue?? pages/ID??. DOI: 10.1021/acsomega.5c11133.

[7] Ziani, S., Aitali, S., Brahmi, A., Zakaria, Y., Zaabar, A., Meski, S., Boudrahem, F., Khireddine, H., Ghernaout, D., Mukalazi, H., Belaadi, A. (2026) A sustainable bioadsorbent approach for tetracycline adsorption from aqueous solutions using calcined chicken bone waste : Optimization via response surface methodology, *Results in Engineering*, 29, 109169. DOI: 10.1016/j.rineng.2026.109169.

[8] Haneem, A., Dom, M., Rezadin, S., Rahim, T.A., Shamsudin, Z. (2024) Influence of Calcination Temperature on the Physicochemical Properties of Synthesized Hydroxyapatite from Cow Bone Waste, journal title?? Vol ??? Issue?? pages/ID??. 1, 115–127. DOI:.....?????

[9] Xin, Y., Kamisaka, Y., Shirai, T. (2025) Elimination of volatile organic compound by hydroxyapatites derived from waste bone biomass, journal title?? Vol ??? Issue?? pages/ID??. 220–224. DOI:.....?

[10] In, Y., Amornkitbamrung, U., Hong, M., Shin, H. (2020) On the Crystallization of Hydroxyapatite under Hydrothermal Conditions: Role of Sebacic Acid as an Additive, *ACS Omega*, 5, 27204–27210. DOI: 10.1021/acsomega.0c03297.

[11] Ishtiaque, S., Das, H. (2022) Synthesis of n-HAP using different precursors and dependence of Vickers hardness on the structure by tuning sintering temperature, *Applied Ceramic Technology*, 19, 1281–1292. DOI: 10.1111/ijac.13964.

[12] Chen, M., Zh, E., Yan, Q., Hu, Z., Xiao, X., Chen, D. (2016) The Effect of Crystal Face of Fe2O3 on the Electrochemical Performance for Lithium-ion Batteries, *Scientific African*, 6, 1–9. DOI: 10.1038/srep29381.

[13] Zhang, X., Li, S., El-Khodary, S.A., Zou, B., Yang, S., Ng, D.H.L., Liu, X., Lian, J. (2020) Huaming, Porous α-Fe2O3 nanoparticles encapsulated within reduced graphene oxide as superior anode for lithium-ion battery, *Nanote*, 31, 145404. DOI:.....?

[14] Chandrasekar, A., Sagadevan, S., Dakshnamoorthy, A. (2013) Synthesis and characterization of nano-hydroxyapatite (n-HAP) using the wet chemical technique, *International Journal of Physical Sciences*, 8, 1639–1645. DOI: 10.5897/IJPS2013.3990.

[15] Goldberg, M.A., Gafurov, M.R., Murzakhanov, F.F., Fomin, A.S., Antonova, O.S., Khairutdinova, D.R., Pyataev, A.V., Makshakova, O.N., Konovalov, A.A., Leonov, A.V., Akhmedova, S.A., Sviridova, I.K., Sergeeva, N.S., Barinov, S.M., Komlev, V.S. (2021) Mesoporous iron(Iii)-doped hydroxyapatite nanopowders obtained via iron oxalate, *Nanomaterials*, 11, 1–21. DOI: 10.3390/nano11030811.

[16] Khan, I., Saeed, K., Zekker, I., Zhang, B., Hendi, A.H., Ahmad, A., Ahmad, S., Zada, N., Ahmad, H., Shah, L.A., Shah, T., Khan, I. (2022) Review on Methylene Blue: Its Properties, Uses, Toxicity and Photodegradation, *Water*, 14, w14020242. DOI: .....???

[17] Demirciog, E., Demir, I. (2021) Effects of Annealing on Structural , Morphological , and Corrosion Properties of a-Fe2O3 Thin Films, *Journal of Electronic Materials*, 50, 2750–2760. DOI: 10.1007/s11664-021-08786-y.

[18] Bredar, A.R.C., Chown, A.L., Burton, A.R., Farnum, B.H. (2020) Electrochemical Impedance Spectroscopy of Metal Oxide Electrodes for Energy Applications, *Applied Energy Materials*, 3, 66–98. DOI: 10.1021/acsaem.9b01965.

[19] Sajid, M.M., Alomayri, T. (2022) Synthesis of α-Fe2O3 rhombus nanoplates for photocatalytic investigation of cationic and anionic dyes and antibacterial aspect, *Journal of Taibah University for Science*, 16, 1192–1201. DOI: 10.1080/16583655.2022.2154094.

[20] Wu, R., Wang, Y., Wang, J., Tian, G., Li, Y., Liu, C. (2025) The, Facile preparation of Fe3O4/HAP/Ag nanomaterial and photocatalytic degradation of four types of dyes with mechanism, *RSC Advances*, 15, 27128–27138. DOI: 10.1039/D5RA03777H.

[21] Bharali, L., Kalita, J., Chakraborty, D., Dhar, S.S., Moyon, N. S. (2023) Hydroxyapatite nanoparticles decorated with metal–organic framework, Co-Cu/ZIF@HAp, and evaluation of photocatalytic performance of the prepared nanocomposite in the degradation of organic pollutants, *Applied Organometallic Chemistry*, 37, e7235. DOI: .....???

[22] Junior, F.E.B., Neves, C.G., Barros, W.R.P. (2022) Photo-Fenton-Based Degradation of Methylene Blue Dye Using Hydroxyapatite Nanoparticles Doped with Fe3O4/γ-Fe2O3, *Journal of Brazilian Chemical Society*, 33, 1441–1455. DOI: .....?????

[23] Mizar, K., Mulyati, S., Aprilia, S., Prayogie, M. (2024) Preparation of tungsten trioxide / graphene oxide / hydroxyapatite (WO3 / GO / HAp) for photocatalytic removal of methylene blue under visible light, *Case Studies in Chemical and Environmental Engineering*, 10, 100870. DOI: 10.1016/j.cscee.2024.100870.

[24] Adhitiyan, T., Dhanaraj, K., Gubendhiran, S., Suresh, G., Thenpandiyan, E., Prasath, M. (2024) Green synthesized silver and zinc doped hydroxyapatite photocatalysts to remove methylene blue and Rhodamine B dyes from industrial wastewater, *Chemical Physics Impact*, 9, pages/ID????. DOI:.....????

[25] Fatimah, I., Fahrani, D., Harmawantika, T., Sahroni, I., Kamari, A., Rahmatillah, C.S., Nurillahi, R. (2019) Functionalization of hydroxyapatite derived from cockle (Anadara granosa) shells into hydroxyapatite–nano TiO2 for photocatalytic degradation of methyl violet, *Sustainable Environment Research*, 1, 1–14. DOI: 10.1186/s42834-019-0034-3.

[26] Fatimah, I., Hidayat, H., Citradewi, P.W., Tamyiz, M., an Doong, R., Sagadevan, S. (2023) Hydrothermally synthesized titanium / hydroxyapatite as photoactive and antibacterial biomaterial, *Heliyon*, 9, e14434. DOI: 10.1016/j.heliyon.2023.e14434.

[27] Arif, S., Fatima, H., Tahir, J., Anwar, M.S. (2025) Doped hydroxyapatite photocatalyst for efficient degradation of Methylene blue dye, *Inorganic Chemistry Communications*, 172, 113684. DOI: 10.1016/j.inoche.2024.113684.

[28] Zheng, X., Yuan, J., Shen, J., Liang, J., Che, J., Tang, B., He, G., Chen, H. (2019) A carnation-like rGO/Bi2O2CO3/BiOCl composite: efficient photocatalyst for the degradation of ciprofloxacin, *Journal of Materials Science: Materials in Electronics*, 30, 5986–5994. DOI: 10.1007/s10854-019-00898-w.

[29] Fatimah, I., Yanti, I., Hana Afiyah Putri, F., Herianto, D., Sagadevan, S., Tamyiz, M., an Doong, R. (2023) Phyto-mediated hydrothermal synthesis of NiFe2O4 as photocatalyst in tetracycline photodegradation, *Environmental Nanotechnology, Monitoring and Management*, 20, 100879. DOI: 10.1016/j.enmm.2023.100879.

[30] Chen, H., Luo, S., Lei, X., Liu, H., Liu, Y., Xu, X.Z. (2020) Jiang, Synthesis and photocatalytic performance of nano-CeO2 by a PVP-assisted microwave interface method for organic dye degradation, *Ionics*, 20, pages/ID????. DOI:..??

[31] Nisrina, A., Karya, T., Halim, R., Murniati, A., Hardian, A., Syarif, D.G. (2024) Evaluation of Mineral-Based Zn-Doped Hydroxyapatite as a Photocatalyst for Methylene Blue Degradation, *Journal of Pure and Applied Chemical Research*, 13, 146–155. DOI: 10.21776/ub.jpacr.2024.013.03.7908.

[32] Khalaji, A.D., Spherical α-Fe2O3 Nanoparticles : Synthesis and Characterization and Its, *Physical Chemistry Research*, 10, 473–483. DOI: 10.22036/PCR.2022.313916.1980.

[33] Goudjil, M.B., Dali, H., Zighmi, S., Mahcene, Z., Bencheikh, S.E. (2024) Photocatalytic degradation of methylene blue dye with biosynthesized Hematite α-Fe2O3 nanoparticles under UV-Irradiation, *Desalination and Water Treatment*, 317, 100079. DOI: 10.1016/j.dwt.2024.100079.

[34] Vu, X.H.O.A., Phuoc, L.H.U.U., Dien, N.D.A.C. (2019) Photocatalytic Degradation of Methylene Blue (MB) over a-Fe2O3 Nanospindles Prepared by a Hydrothermal Route, *Journal of Electronic Materials*, 48, 2978–2985. DOI: 10.1007/s11664-019-07056-2.